Applied Surface Science 513 (2020) 145812

Contents lists available at ScienceDirect

Applied Surface Science

journal homepage: www.elsevier.com/locate/apsusc

Full Length Article

Electronic passivation of PbSe quantum dot solids by trimethylaluminum vapor dosing

Scott T. Ueda[a], Iljo Kwak[a], Alex Abelson[b], Steven Wolf[a], Caroline Qian[c], Matt Law[d,b,c], Andrew C. Kummel[a,*]

[a] Materials Science and Engineering Program and Department of Chemistry and Biochemistry, University of California, San Diego, La Jolla, CA 92093, United States
[b] Department of Materials Science and Engineering, University of California, Irvine, Irvine, CA 92697, United States
[c] Department of Chemical and Biomolecular Engineering, University of California, Irvine, Irvine, CA 92697, United States
[d] Department of Chemistry, University of California, Irvine, Irvine, CA 92697, United States

ARTICLE INFO

Keywords:
PbSe
Quantum dots
Nanocrystals
Passivation
Scanning tunneling microscopy (STM)
Scanning tunneling spectroscopy (STS)
Field-effect transistors

ABSTRACT

The inherent instability of PbSe quantum dot (QD) thin films in ambient atmospheric conditions presents a significant challenge to their use in devices. Using low-temperature scanning tunneling microscopy and scanning tunneling spectroscopy, the electronic passivation of epitaxially-fused PbSe QD superlattices (epi-SLs) by trimethylaluminum (TMA) vapor dosing was studied. TMA dosing immobilizes loosely bound mobile adsorbates and passivates states on the surface of the QDs. X-ray photoelectron spectra of QD films prepared by dip coating show an aluminum surface concentration of <1% of a monolayer, consistent with the TMA binding only to defect sites. Field-effect transistor (FET) transport measurements of similar films confirm the impact of this trace surface state passivation. QD FETs dosed with TMA show a shift from *p*-channel to *n*-channel behavior as well as a 20-fold increase in mobility and 300-fold increase in on/off ratio compared to devices before TMA dosing. Defect passivation by TMA vapor dosing may facilitate the integration of PbSe QD solids into future optoelectronic devices.

1. Introduction

Lead chalcogenide (PbX, where X = S, Se, or Te) quantum dots (QDs) are of interest for next-generation electronic and optoelectronic devices due to their tunable optical and electrical properties and enhanced ability to generate multiple excitons per photon compared to their bulk semiconductor counterparts [1–4]. Enhanced multiple exciton generation (MEG) opens the door to highly-efficient photovoltaics, and several groups report efficient MEG for colloidal PbX systems [5–9]. Superlattices (SLs) composed of "confined-but-connected" or "epitaxially fused" QDs (epi-SLs) are expected to generate bulk-like electronic mini-bands and exhibit high carrier mobility and diffusion length compared to conventional weakly-coupled QD solids [2,10,11]. Physical and electronic coupling between the QDs is achieved by exchange of oleate ligands with smaller ligands such as SCN^-, S^{2-}, or ethylene glycoxide that cause necking (limited crystallographic fusion) of the QDs [12–15]. Despite strong electronic coupling, charge transport in epi-SLs can be severely limited by surface states [16] arising from undercoordinated surface atoms, non-stoichiometry, ligands, weakly-bound adsorbates, or oxidation [17–19].

In this work, the local densities of states of monolayer (2D) and bilayer epi-SLs of PbSe QDs were measured by low-temperature scanning tunneling microscopy/spectroscopy (STM/STS) in ultra-high vacuum (UHV), and it was demonstrated that *in vacuo* dosing with trimethylaluminum (TMA) vapor improves STM imaging and passivates surface states to yield an electronically unpinned QD surface. X-ray photoelectron spectra of similar TMA-dosed samples showed a very small aluminum coverage (<1% of a monolayer), indicating that TMA binds to only a small fraction of surface sites, which was hypothesized to be the most active surface defect states. TMA dosing also improved the performance of PbSe QD field-effect transistors (FETs). TMA-dosed FETs showed a shift from *p*-channel to *n*-channel behavior as well as a 20-fold increase in mobility and 300-fold increase in on/off ratio compared to devices without TMA dosing.

2. Methods

2.1. Materials

All chemicals were used as received unless otherwise noted. Lead

* Corresponding author.
E-mail address: akummel@ucsd.edu (A.C. Kummel).

https://doi.org/10.1016/j.apsusc.2020.145812
Received 23 November 2019; Received in revised form 3 February 2020; Accepted 15 February 2020
Available online 16 February 2020

oxide (PbO, 99.999%) and selenium shot (99.999%) were purchased from Alfa Aesar. Trimethylaluminum (TMA, 98%) was purchased from both Strem Chemicals and Sigma Aldrich. Oleic acid (OA, technical grade, 90%), 1-octadecene (ODE, 90%), diphenylphospine (DPP, 98%), anhydrous hexanes (99%), anhydrous ethanol (99.5%), anhydrous toluene (99.8%), anhydrous octane (≥99%), anhydrous acetonitrile (99.99%), anhydrous isopropanol (IPA, 99.5%), anhydrous tetrachloroethylene (TCE, 99%), acetone (99.9%), ammonium thiocyanate (NH_4SCN, 99.99%), and 3-mercaptopropyltrimethoxysilane (3-MPTMS, 95%) were purchased from Sigma Aldrich. Trioctylphosphine (TOP, technical grade, >90%) was purchased from Fluka and mixed with selenium shot over a period of 24 h to create a 1 M TOP-Se stock solution. Prior to use, the NH_4SCN was purified via recrystallization in anhydrous isopropanol.

2.2. Quantum dot synthesis

Oleate-capped PbSe quantum dots with a diameter of 6.5 nm were synthesized using standard air-free techniques. In a typical synthesis, PbO (1.5 g), oleic acid (5.0 g), and ODE (10.0 g) were mixed and degassed thoroughly in a three-neck round-bottom flask at room temperature. The mixture was heated to 110 °C in vacuum to form $Pb(OA)_2$ and to dry the solution. After 1.5 h, the $Pb(OA)_2$ solution was heated to 180 °C in flowing argon, then 9.5 mL of a 1 M solution of TOP-Se containing 200 μL of DPP was rapidly injected into the hot solution. The QDs were grown at ~150 °C for 105 s, at which point the reaction was quenched with a liquid nitrogen bath and the injection of 10 mL of anhydrous hexanes. The QDs were purified in a N_2-filled glovebox (<0.5 ppm O_2) by three rounds of precipitation/redispersion using ethanol/hexane, then dispersed in toluene (1.75 g L^{-1}) for film fabrication.

2.3. Basic characterization

Optical extinction measurements of QDs dispersed in TCE were performed air-free with a PerkinElmer Lambda 950 spectrophotometer. Neat TCE served as the background for the solution measurements. The QD diameter and polydispersity were determined using the empirical relationship of Moreels et al. [20]. Scanning electron microscopy (SEM) was performed on an FEI Magellan 400L SEM operating at 10 kV and 25 pA.

Small angle X-ray scattering (SAXS) measurements were performed on Beamline 7.3.3 of the Advanced Light Source (ALS) at Lawrence Berkeley National Laboratory using 10 KeV monochromatic X-rays (λ = 1.24 Å) with an energy bandwidth of 1%. A Dectris Pilatus 2 M detector with a pixel size of 0.172 × 0.172 mm and 1475 × 1679 pixels was used to record the 2D scattering patterns. A silver behenate standard was used to determine the sample-to-detector distance and beam center. For solution SAXS measurements, a 30 gL^{-1} octane suspension of QDs was drawn into a 2 mm × 0.2 mm glass capillary with a 0.150 mm wall thickness (Electron Microscopy Sciences). The solution was exposed to air briefly before and during measurement. The sample-to-detector distance was 2994.78 mm as calibrated by the silver behenate standard. Signal was collected for 120 s, and an octane-filled blank capillary was used for background subtraction. The Nika software package [21] in Igor Pro was used to azimuthally integrate (25–75°) the SAXS pattern and correct for the background using the octane-filled blank. Particle distribution fitting was performed using a spherical form factor with a Gaussian spread of QD diameters in the NIST SANS Analysis package [22] in Igor Pro. No instrumental broadening was included in the fitting procedure, which indicates that the reported polydispersity is likely an overestimation.

2.4. Scanning tunneling microscopy

Sub-monolayer QD films were prepared by dip coating in a N_2-filled glovebox (<5 ppm O_2) adjacent to the STM instrument. First, oleate-capped PbSe QDs dispersed in toluene were dip coated onto a mechanically-exfoliated highly oriented pyrolytic graphite (HOPG) substrate. Once the toluene fully evaporated, the substrate was immersed in a 4 mM solution of NH_4SCN in acetone to trigger ligand exchange and epi-SL formation. The substrate was rinsed for 10 s in anhydrous acetonitrile, hexane, and again in acetonitrile to remove free ligands, dried, and transferred into a commercial Omicron VT UHV STM (base pressure = 1×10^{-11} Torr) using a glove bag purged with N_2 to avoid air exposure. These samples were first measured before TMA exposure, then transferred *in vacuo* to an attached ALD chamber (base pressure ~10^{-6} Torr), dosed with TMA using multiple 350 mTorr pulses (total TMA dose of 2–8 × 10^6 Langmuir), and transferred back to the STM chamber without air exposure.

STM topography images were acquired with a tungsten tip prepared by electrochemical etching of a tungsten wire. Images were acquired at 100 K in constant current mode (I = 0.03 nA) with a tip bias of +2 V. Scanning tunneling spectroscopy (STS) was performed at 100 K to investigate the electronic structure of the QDs using variable z-mode over a bias range of −1 to 1 V. To determine the onset bias relative to the Fermi level (i.e., the valence and conduction band edge energies) from the $(dI/dV)/(I/V)$ curves, STS curve fitting was employed as described in detail by Feenstra et al. [23,24].

2.5. X-ray photoelectron spectroscopy

Multilayer QD films for XPS characterization were deposited by manual layer-by-layer dip coating [25] at UC San Diego using the same NH_4SCN solution used to fabricate the STM/STS samples. These discontinuous films were amorphous (i.e., minimal QD positional order and epi-SL grains). The samples were transferred with minimal air exposure via glove bag to a monochromatic XPS system (Al Kα, $h\nu$ = 1486.7 eV). XP spectra were acquired at a collection angle of 60° relative to the surface normal at a pass energy of 50 eV and step width of 0.1 eV. Analysis of the XPS data was performed in CasaXPS v2.3 using Shirley background subtraction and Schofield photoionization cross sectional relative sensitivity factors.

2.6. Field-effect transistor measurements

Multilayer QD film field-effect transistor (FETs) employed a bottom contact (5 nm Ti, 35 nm Au), global back gate geometry (p^{++} Si, 200 nm SiO_2, C_{ox} = 17.5 nF/cm^2) with a channel length of 25 μm and width of 1000 μm. FET substrates were cleaned by successive sonication in acetone, Millipore water, and IPA, blown dry with air, then treated with 15 min of O_2 plasma cleaning. The substrates were transferred into the glovebox and soaked in a 100 mM solution of 3-MPTMS in toluene for 1 h to improve QD adhesion, rinsed vigorously in neat toluene and dried in flowing nitrogen. Automated layer-by-layer dip coating of QD films was performed at UC Irvine using a Nima DC-4 dip coater in the glovebox. Substrates were dipped into a 3.9 gL^{-1} dispersion of QDs in hexane, followed by a 12 s soak in a 15 mM solution of NH_4SCN in acetonitrile and finally a 3 s soak in neat acetonitrile. This process was repeated 10 times to generate ~40 nm thick QD films. The FETs were dosed with TMA in a low-vacuum ALD system (base pressure ~10^{-2} Torr) integrated into the glovebox. TMA was dosed for 100 ms (10^5–10^6 Langmuir) using a computer-controlled diaphragm valve. FETs were measured in the glovebox (<0.1 ppm O_2) using a Keithley 2636B source-measure unit controlled by home-built LabView software. All measurements were performed at room temperature using a sweep rate of ~40 V/s to minimize artifacts from the bias-stress effect.

3. Results and discussion

Fig. 1a shows an optical extinction spectrum of a suspension of the oleate-capped PbSe QDs used in this study (diameter of 6.6 ± 0.4 nm,

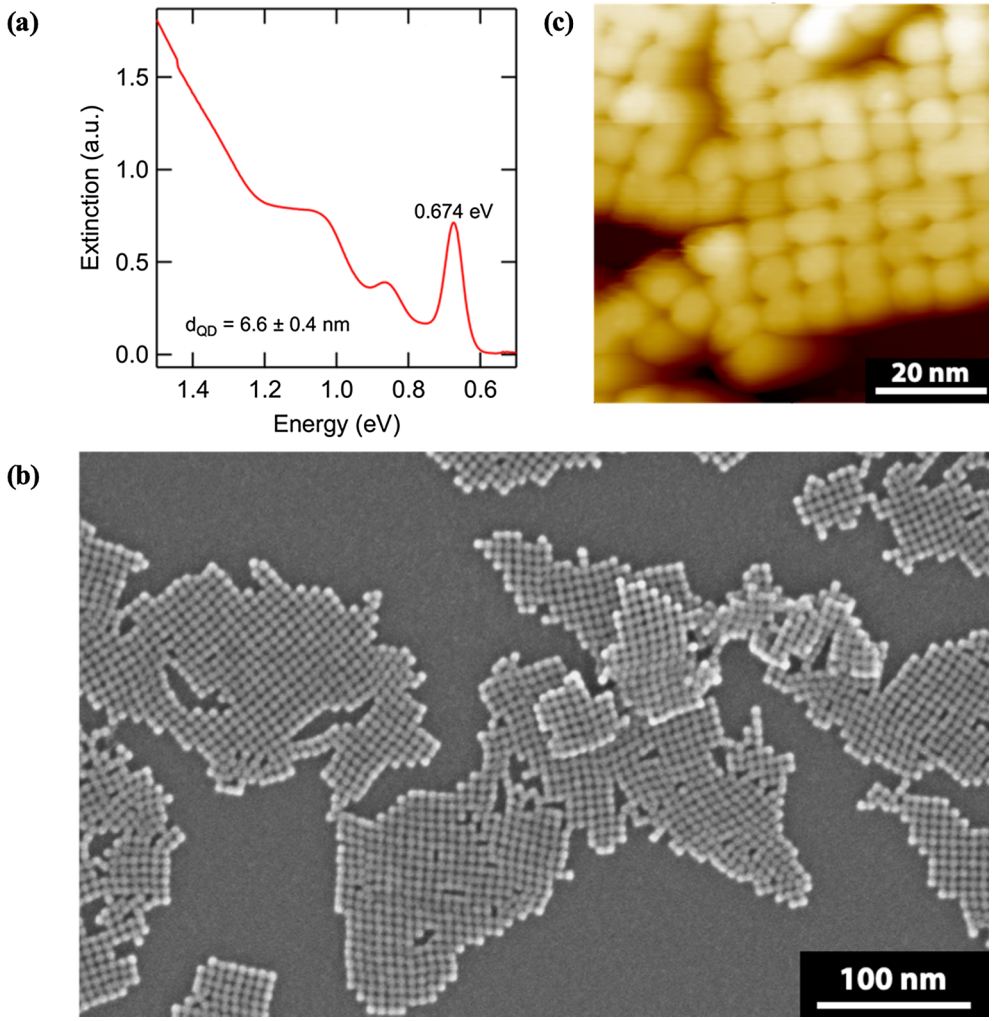

Fig. 1. The PbSe QD epitaxial superlattices studied by STM. (a) Optical extinction spectrum of the PbSe QDs dispersed in tetrachloroethylene. (b) Representative SEM image of 2D epi-SL grains on HOPG. (c) Corresponding STM topography image.

band gap of 0.674 eV). The QD diameter was determined using both small angle X-ray scattering (Fig. S1 in the Supporting Information) and the empirical sizing curve of Moreels et al. [20]. Sub-monolayer to bilayer thick films of these QDs were formed by controlled evaporation of a toluene suspension on freshly exfoliated highly-oriented pyrrolitic graphite (HOPG) substrates (see Methods). Once dry, the samples were immersed in a solution of ammonium thiocyanate in acetone to exchange the native oleate ligands and generate the epitaxially-fused SLs shown by SEM imaging in Fig. 1b [26]. These samples feature small (10–100 nm) 2D epi-SL grains scattered across the substrate. The SL grains consist of 1–2 monolayers of QDs that are epitaxially connected across their {1 0 0} facets to form quasi-square lattices, similar to the structure of previously-reported 2D epi-SLs [27,28]. Fig. 1c is a representative scanning tunneling microscopy (STM) topography image of a smaller area of one of these samples showing that the quasi-square SL is clearly resolved.

Fig. 2 presents STM images of an epi-SL sample before and after *in vacuo* dosing with 2×10^6 L of TMA vapor at room temperature. Before TMA dosing, the STM images exhibited temporal instability, scan artifacts, and high noise (Fig. 2a). After dosing, STM image quality was significantly enhanced (Fig. 2b). The improvement was quantified by measurement of the RMS surface roughness averaged over several QDs, which decreased from 0.28 to 0.15 nm. An increase in noise when surface adsorbates attach to STM tips is a well-known phenomenon that likely arises from adsorbates on the tip changing conformation during the scan, leading to instabilities in the tunneling current [29]. Therefore, the improved image sharpness and decrease in RMS roughness is attributed to TMA-facilitated immobilization or removal of weakly-bound adsorbates such as physisorbed water and hydroxyl groups.

The local density of states (LDOS) of 40 QDs in the monolayer epi-SL grains was measured as a function of TMA dosing (Fig. 3). STS traces were acquired at the center of the top {1 0 0} facet of each QD. Qualitative comparison of the normalized differential conductance (dI/dV)/(I/V) versus voltage traces before and after TMA dosing shows that the TMA treatment significantly increases the electrical band gap of the QDs (Fig. 3a). The band gap value were calculated from fits of the STS data following Feenstra et al. [23,24]. Before TMA dosing, the measured band gap is 0.35 ± 0.07 eV, which is 0.32 eV smaller than the optical band gap of the QDs in solution (Fig. 1a) and 0.30 eV smaller than the optical band gap of the ligand-exchanged QD films. Fig. 3b plots the electrical band gap versus the TMA dose. The band gap increases with increasing TMA dose until a dose of ~5×10^6 L, where it saturates at 0.65 ± 0.06 eV, close to the value of the optical band gap (Fig. 3b). This behavior is consistent with the passivation of gap states by TMA, ostensibly via the reduction of trace selenium oxides that are known to create defect states and dangling bonds on PbSe QDs [17,18,30]. Defect-induced band gap narrowing has been found on many other surfaces, including PbS QDs [31], where density functional theory was used to model the generation of weakly-conductive midgap states caused by Pb:S off-stoichiometry, and Ge(100), where STM/STS

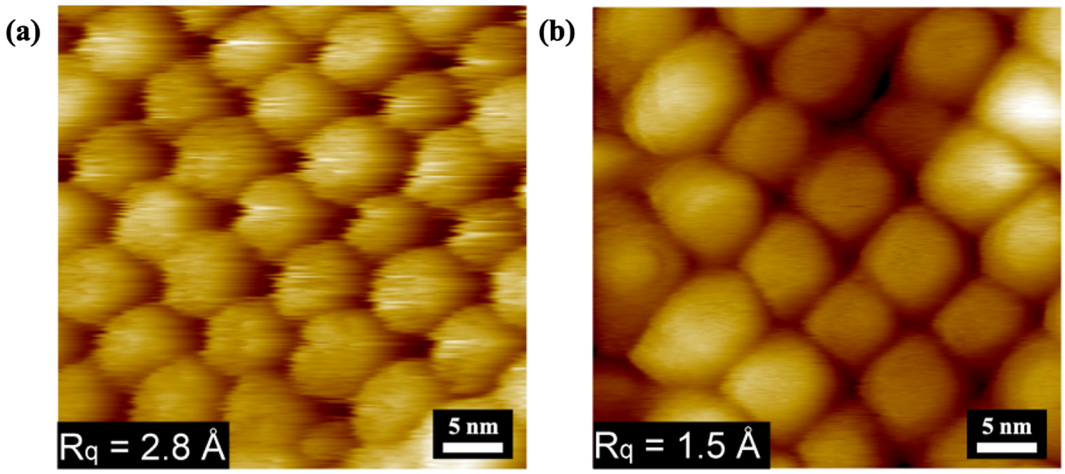

Fig. 2. Effect of TMA dosing on STM image quality. STM images acquired at 100 K in constant current mode (I = 0.03 nA) with a tip bias of +2 V (a) before and (b) after TMA dosing (2×10^6 L in high vacuum) and their corresponding RMS roughness values (R_q). TMA dosing improves imaging, consistent with the immobilization or removal of loosely-bound adsorbates that interfere with the STM tip.

was used to investigate H_2O_2 passivation of Ge dangling bonds [32].

Fig. 4a–d show pre- and post-TMA STS curves from mono- and bilayer portions of the QD SL. The extracted difference between the intrinsic Fermi level and measured Fermi level of each sample (E_i-E_F) is compiled in Fig. 4e. The total TMA dose was approximately 5×10^6 L, which is the same dose required to restore the band gap (see Fig. 3). STS traces were recorded on tens of QDs in each layer before and after dosing. Before TMA dosing, the QDs displayed predominantly *p*-type behavior (E_i-E_F = 0.11 ± 0.08 eV with E_g = 0.35 eV) in monolayer portions of the films and E_i–E_F = 0.14 ± 0.07 eV in bilayers (Fig. 4a–b). After TMA dosing, QDs in the monolayer became intrinsic (E_i-E_F = 0.05 ± 0.11 eV with E_g = 0.65 eV) while those in the bilayer remained *p*-type (E_i-E_F = 0.22 ± 0.06 eV). This Fermi level difference is consistent with band bending at the QD-HOPG interface. Prior to TMA treatment, the Fermi level may be pinned by surface defects (e.g., surface oxides), as was reported previously [33,34]. Following TMA treatment, the surface states are passivated, and the Fermi level becomes unpinned. Fig. 4f–g show band diagrams for both situations. Due to the smaller work function of the HOPG substrate relative to the QDs, downward band bending will occur in the QD layer when the Fermi level is unpinned (Fig. 4f). This band bending causes QDs in the first monolayer (at the QD-HOPG interface) to appear more intrinsic while those in the second monolayer appear more *p*-type, in line with our measurements of TMA-dosed samples. However, if the Fermi level is pinned by surface states with energies near the valence band edge, then E_i-E_F should be independent of QD layer, as observed for samples before TMA dosing (Fig. 4g).

X-ray photoelectron spectroscopy was performed to determine the coverage of TMA reaction products on the surface of multilayer QD films made by dip coating (see Methods). Multilayer amorphous films were used for XPS because the mono-/bi-layer films used for STM/STS studies were too sparse to produce high signal-to-noise XP spectra. Fig. 5 shows high-resolution XP spectra of the Pb 4f, Se 3d, O 1s, and Al 2p regions and quantification of the detected elements (Pb, Se, and C). It was expected that Al from TMA would bind to the surface of the QDs and be detectable by XPS. However, no aluminum or oxygen signal was observed before or after TMA dosing (Fig. 5d–e). Although there is no detectable oxygen and the chemical shift of Pb and Se suggest purely Pb-Se bonding without a large coverage of surface oxides, oxygen is a known acceptor in PbX QD films [35,36] and can likely dope the QDs at concentrations below the detection limit of XPS [17,37–41]. The absence of oxygen signal, the chemical shift of the carbon peak (Fig. 5c), and SEM imaging of an identically prepared sample (Fig. S2) indicate that the large carbon signal originates from the HOPG substrate and not

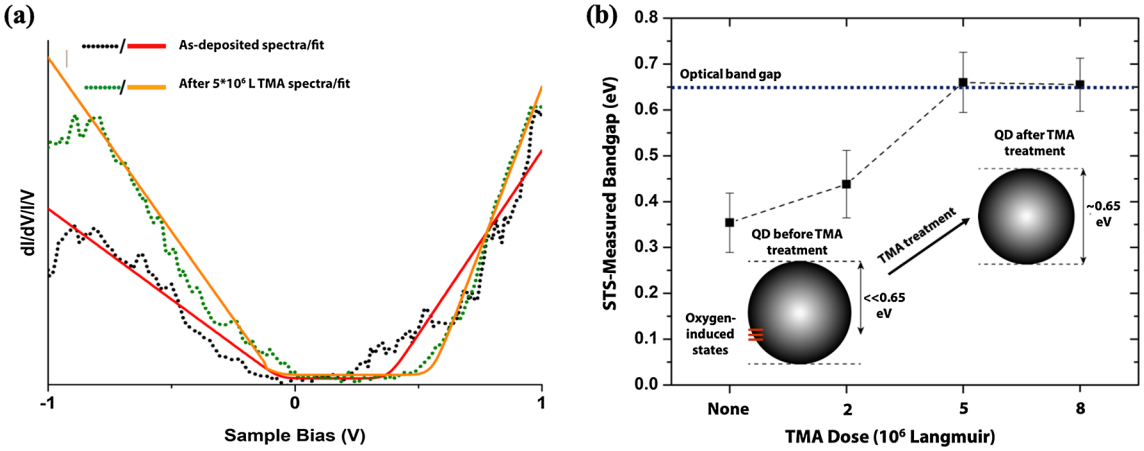

Fig. 3. Effect of TMA dosing on QD band gap. (a) Representative ST spectra (dashed lines) and fits (solid lines) for a PbSe QD before (red) and after (orange) a 5×10^6 L dose of TMA. (b) Before TMA dosing, the STS-measured band gap of QDs in monolayer epi-SLs is only 0.35 ± 0.07 eV (avg ± 1 SD), much smaller than the optical band gap of the QD films (~0.65 eV). The band gap increases with increasing TMA dose until it saturates at 0.65 ± 0.06 eV, close to the value of the optical band gap. This behavior is consistent with the passivation of gap states by TMA. (For interpretation of the references to colour in this figure legend, the reader is referred to the web version of this article.)

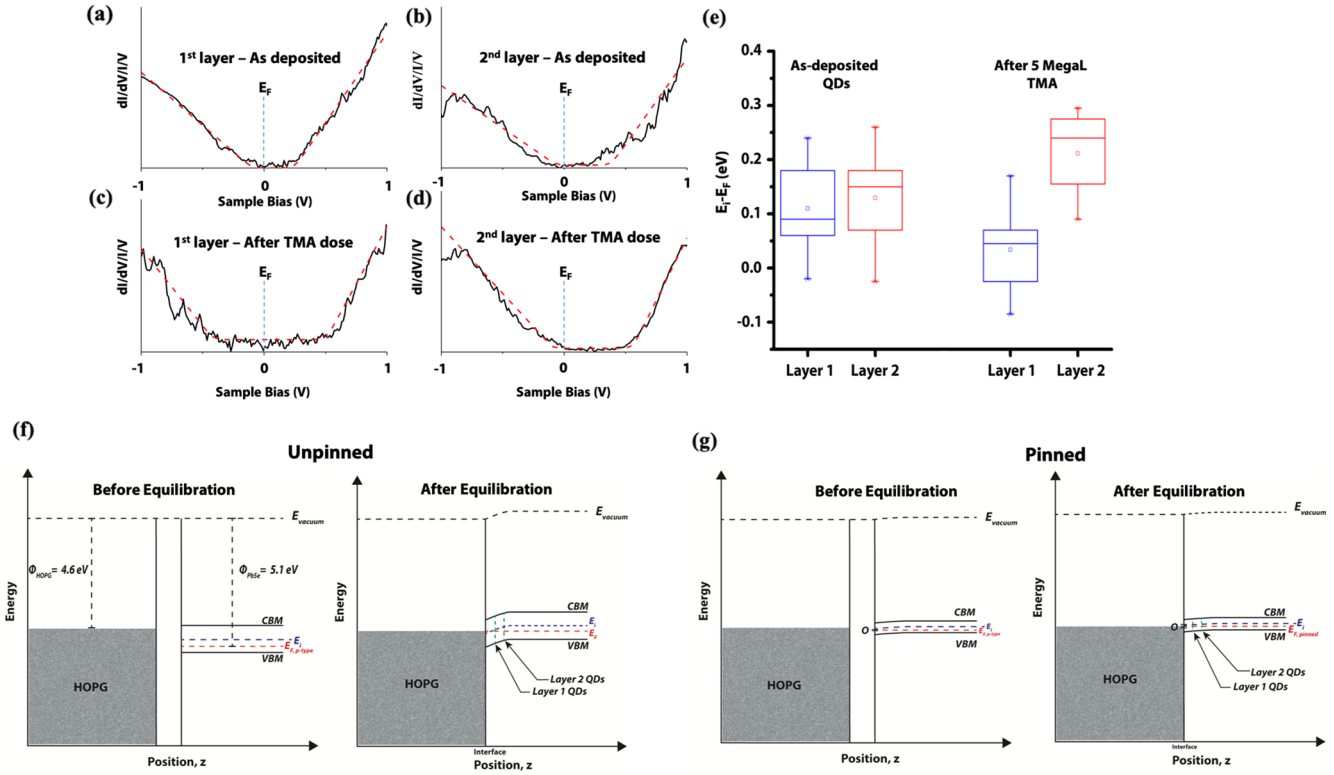

Fig. 4. Effect of TMA dosing on the Fermi level of QDs in the first and second QD monolayers. (a, b) Typical STS data (solid black lines) and fits [23,24] (dashed red lines) of TMA-treated QDs in the (a) first and (b) second QD monolayers on the HOPG substrate. The Fermi level of QDs in the first monolayer (Layer 1) is located near the middle of the band gap, while the Fermi level of QDs in the second monolayer (Layer 2) is significantly closer to the valence band edge (*p*-type). **(c, d)** Typical STS data (black) and fits (red) for QDs before TMA treatment, showing that QDs in the two layers have similar Fermi levels close to the valence band edge (*p*-type). **(e)** The relative Fermi level (E_i-E_F) of QDs in the two layers before and after TMA dosing. Each line in the boxplot represents a quartile, with the middle line representing the data median. The small square denotes the average of the dataset while the whiskers denote the full data range. **(f, g)** Schematic band diagrams of the HOPG-QD system (f) with and (g) without TMA dosing. With dosing, QD surface states are passivated and the Fermi level is unpinned, resulting in downward band bending in the QD film after equilibration with HOPG and Fermi level positons near mid gap for QDs in the first monolayer and closer to the valence band edge for QDs in the second monolayer. Without dosing, QD surface states pin the Fermi level near the valence band edge, yielding very similar Fermi level positions for QDs in the two monolayers after equilibration with HOPG. (For interpretation of the references to colour in this figure legend, the reader is referred to the web version of this article.)

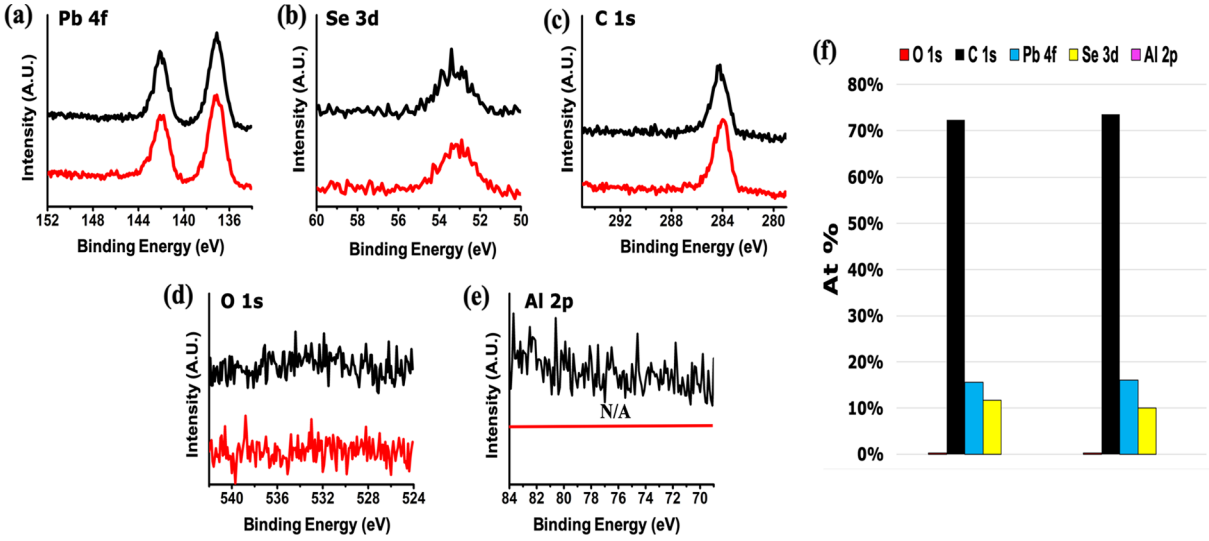

Fig. 5. XP spectra before and after TMA dosing. (a–e) High-resolution XP spectra of (a) Pb 4f, (b) Se 3d, (c) Al 2p, (d) O 1s, and (e) C 1s before (red) and after (black) TMA dosing (10^7 L). Al and O are below XPS detection limits, demonstrating that nearly all of the QD surface sites are unreactive towards TMA. Pb and Se show no evidence for oxide formation. (f) Sample surface composition before and after TMA dosing. (For interpretation of the references to colour in this figure legend, the reader is referred to the web version of this article.)

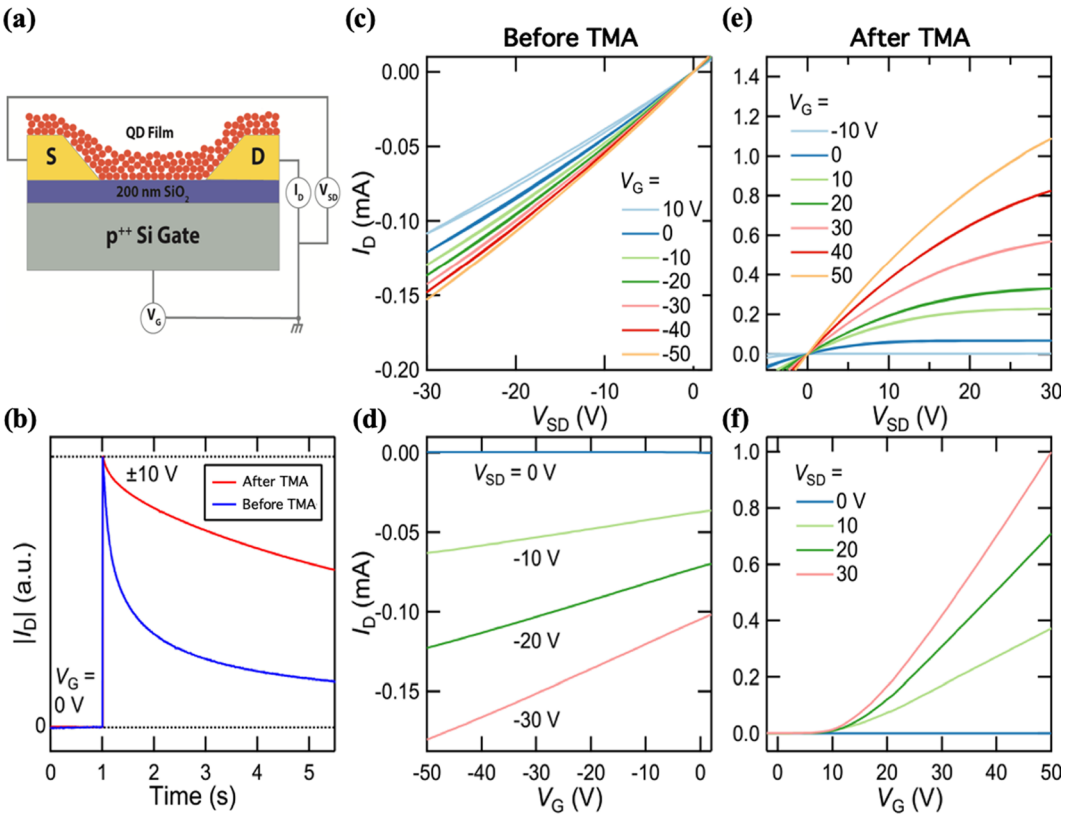

Fig. 6. Impact of TMA dosing on charge transport in QD field-effect transistors. (a) Schematic of the FET geometry. (b) Normalized drain current for a FET before and after TMA dosing. The applied source-drain bias was −10 V before dosing and +10 V after dosing. The data were normalized to equalize the change in drain current induced by a ±10 V gate bias (negative before dosing and positive after dosing). (c) Output and (d) transfer curves for the FET before TMA dosing. (e) Output and (f) transfer curves immediately after exposure to TMA.

residual oleate ligands or adventitious hydrocarbons. The XPS data are consistent with TMA passivating surface states and/or removing ligands with a density below 10^{13} cm^{-2}, which is 10× more than required to pin the Fermi level but still below the detection limit of XPS [42].

A simple thermodynamic analysis can be employed to show that TMA is likely to react with all surface oxides. The primary oxidation products of PbSe QDs are PbO, SeO_2, and $PbSeO_3$, as shown in Eqs. (1)–(3):[18,43,44]

$$PbSe(s) + 1.5O_2(g) \rightarrow PbO(s) + SeO_2(s) \quad (1)$$

$$PbSe(s) + 1.5O_2(g) \rightarrow PbSeO_3(s) \quad (2)$$

$$PbSe(s) + O_2(g) \rightarrow Pb(s) + SeO_2(s) \quad (3)$$

Proposed mechanisms for the surface reaction of TMA and reduction of trace surface oxides are the following:

$$1.5SeO_2(s) + 2Al(CH_3)_3(g) \rightarrow 3C_2H_6(g) + 1.5Se(s) + Al_2O_3(s) \quad (4)$$

$$PbSeO_3(s) + 2Al(CH_3)_3(g) \rightarrow 3C_2H_6(g) + Se(s) + Pb(s) + Al_2O_3(s) \quad (5)$$

$$3PbO(s) + 2Al(CH_3)_3(g) \rightarrow 3C_2H_6(g) + 3Pb(s) + Al_2O_3(s) \quad (6)$$

In reactions (4)–(6), the primary driving force for the reduction of surface oxides is the formation of aluminum oxide. Using known heats of formation, the reaction enthalpies for reactions (4)–(6) are calculated to be −1392 kJ/mol, −1217 kJ/mol, and −1091 kJ/mol indicating it is thermodynamically favored for TMA to react with all three of the common oxidation products on the surface of the QDs, thereby passivating defect states that are known to arise from the presence of mixed Se-containing oxides [19,30]. The electronic passivation of semiconductor surfaces via the reduction or removal of surface oxides and adsorbed water by TMA is favored by the large formation enthalpy of Al_2O_3 and is consistent with the so-called "TMA clean-up effect" observed for many semiconductors including GaAs [45,46], InAs [47], and Ge [48].

Field-effect transistors (FETs) were fabricated to independently assess the impact of TMA dosing on the electronic properties of multilayer QD films. A cartoon of the FET geometry is provided in Fig. 6a. Pre-TMA devices exhibited significant drain current transients (Fig. 6b) resulting from the bias-stress effect [49]. Fig. 6c–d show output and transfer characteristics of these devices, which were *p*-channel with I_{on}/I_{off} = 1.5 (at V_{SD} = −10 V and V_G = 0 vs. −40 V) and a linear hole mobility $\mu_{lin,h}$ = 0.07 cm^2/Vs. The FETs were dosed with TMA and immediately remeasured. These TMA-treated FETs (Fig. 6e–f) were dominant *n*-channel devices, with I_{on}/I_{off} = 440, $\mu_{lin,e}$ = 1.4 cm^2/Vs, and with improved drain current stability (see Fig. 6b). The 20-fold increase in mobility is likely due to the change in carrier polarity [50] and removal of in-gap defect states by TMA, in agreement with the STM/STS results demonstrating an unpinned Fermi level following TMA exposure. The 300-fold increase in on/off ratio results primarily from a decrease in I_{off} that we attribute to the passivation of shallow defect states associated with trace surface oxides.

Similarly large increases in mobility have been observed by passivating trap states in transition metal chalcogenide QD devices using methods such as indium diffusion doping of CdSe QDs [51] and ALD alumina infilling of PbSe QDs [16]. However, this study is unique because it shows that trace amounts of surface oxidation (below XPS detection limits) are present even on ligand-exchanged QDs fabricated using "air-free" techniques and that TMA can effectively repair these defects. Additional experiments on PbSe QDs treated with 1,2-ethanedithiol (EDT) instead of NH_4SCN demonstrate a comparatively minor improvement in FET performance (see Fig. S3). The FET data in Fig. 6 are consistent with TMA eliminating surface oxidation products that

result from exposure to trace oxygen and water during QD synthesis, purification, and storage [52]. These surface oxides generate high conductivity and *p*-channel behavior in PbSe QD films, which is in agreement with both the *p*-type behavior observed prior to dosing in the STS studies and the FET data [40]. By eliminating trace defect states with TMA dosing, both the carrier mobility and on/off ratio increase by 1–2 orders of magnitude.

4. Conclusions

TMA dosing provides a facile means to remove trace surface oxides on PbSe QD films and yields insight into the origin and impact of electronic defects in these materials. Dosing with TMA was found to improve STM image quality, passivate defects, widen the local band gap, unpin the Fermi level, and improve charge transport and transistor performance, consistent with the removal of surface oxides and/or adsorbates present at coverages below 1% of a monolayer. XP spectra lacked Al and O signal following defect removal by TMA, demonstrating the low surface density of these defect states. Transistors were used to show the impact of this trace defect removal on charge transport. FETs exposed to TMA show a shift from *p*-channel to *n*-channel behavior as well as large increases mobility and on/off ratio compared to devices without TMA treatment. The data suggest that trace coverages of oxides and other adsorbate dopants (e.g., water) have a strong impact on electrical transport within these QD films. The demonstration of TMA passivation in these studies highlights the importance of developing passivation techniques to improve the design of QD solids for eventual integration into electronic devices and shows that an order of magnitude improvement in QD device performance can be obtained by effectively passivating these trace defect states.

Author contributions

Scott T. Ueda: Data curation, Methodology, Formal analysis, Investigation, Writing - original draft, Writing - review and editing, and Visualization. **Iljo Kwak:** Data curation, Methodology, Formal analysis, and Investigation. **Alex Abelson:** Data curation, Methodology, Formal analysis, Investigation, and Writing - review and editing. **Steven Wolf:** Data curation and Investigation. **Caroline Qian:** Data curation, Investigation, and Writing - review and editing. **Matt Law** and **Andrew C. Kummel:** Conceptualization, Funding acquisition, Supervision, Writing - review & editing, and Project administration.

Declaration of Competing Interest

The authors declare that they have no known competing financial interests or personal relationships that could have appeared to influence the work reported in this paper.

Acknowledgement

This work was supported by the UC Office of the President under the UC Laboratory Fees Research Program Collaborative Research and Training Award LFR-17-477148. This research used resources of the Advanced Light Source, which is a DOE Office of Science User Facility under contract no. DE-AC02-05CH11231.

Appendix A. Supplementary material

Supplementary data to this article can be found online at https://doi.org/10.1016/j.apsusc.2020.145812.

References

[1] P.V. Kamat, Quantum dot solar cells. Semiconductor nanocrystals as light harvesters, J. Phys. Chem. C (2008), https://doi.org/10.1021/jp806791s.

[2] A.J. Nozik, M.C. Beard, J.M. Luther, M. Law, R.J. Ellingson, J.C. Johnson, Semiconductor quantum dots and quantum dot arrays and applications of multiple exciton generation to third-generation photovoltaic solar cells, Chem. Rev. (2010), https://doi.org/10.1021/cr900289f.

[3] A.G. Midgett, J.M. Luther, J.T. Stewart, D.K. Smith, L.A. Padilha, V.I. Klimov, A.J. Nozik, M.C. Beard, Size and composition dependent multiple exciton generation efficiency in PbS, PbSe, and PbSxSe1-x alloyed quantum dots, Nano Lett. (2013), https://doi.org/10.1021/nl4009748.

[4] M.C. Beard, A.G. Midgett, M.C. Hanna, J.M. Luther, B.K. Hughes, A.J. Nozik, Comparing multiple exciton generation in quantum dots to impact ionization in bulk semiconductors: implications for enhancement of solar energy conversion, Nano Lett. (2010), https://doi.org/10.1021/nl101490z.

[5] R.D. Schaller, V.I. Klimov, High efficiency carrier multiplication in PbSe nanocrystals: implications for solar energy conversion, Phys. Rev. Lett. (2004), https://doi.org/10.1103/PhysRevLett. 92.186601.

[6] R.J. Ellingson, M.C. Beard, J.C. Johnson, P. Yu, O.I. Micic, A.J. Nozik, A. Shabaev, A.L. Efros, Highly efficient multiple exciton generation in colloidal PbSe and PbS quantum dots, Nano Lett. (2005), https://doi.org/10.1021/nl0502672.

[7] J. Minbiao, P. Sungnam, S.T. Connor, T. Mokari, C. Yi, K.J. Gaffney, Efficient multiple exciton generation observed in colloidal PbSe quantum dots with temporally and spectrally resolved intraband excitation, Nano Lett. (2009), https://doi.org/10.1021/nl900103f.

[8] M.T. Trinh, A.J. Houtepen, J.M. Schins, J. Piris, L.D.A. Siebbeles, Nature of the second optical transition in PbSe nanocrystals, Nano Lett. (2008), https://doi.org/10.1021/nl8010963.

[9] J.E. Murphy, M.C. Beard, A.G. Norman, S.P. Ahrenkiel, J.C. Johnson, P. Yu, O.I. Mićić, R.J. Ellingson, A.J. Nozik, PbTe colloidal nanocrystals: synthesis, characterization, and multiple exciton generation, J. Am. Chem. Soc. (2006), https://doi.org/10.1021/ja0574973.

[10] E. Kalesaki, W.H. Evers, G. Allan, D. Vanmaekelbergh, C. Delerue, Electronic structure of atomically coherent square semiconductor superlattices with dimensionality below two, Phys. Rev. B – Condens. Matter Mater. Phys. (2013), https://doi.org/10.1103/PhysRevB.88.115431.

[11] C.R. Kagan, C.B. Murray, Charge transport in strongly coupled quantum dot solids, Nat. Nanotechnol. (2015), https://doi.org/10.1038/nnano.2015.247.

[12] A.T. Fafarman, W.K. Koh, B.T. Diroll, D.K. Kim, D.K. Ko, S.J. Oh, X. Ye, V. Doan-Nguyen, M.R. Crump, D.C. Reifsnyder, et al., Thiocyanate-capped nanocrystal colloids: vibrational reporter of surface chemistry and solution-based route to enhanced coupling in nanocrystal solids, J. Am. Chem. Soc. (2011), https://doi.org/10.1021/ja206303g.

[13] J. Tang, K.W. Kemp, S. Hoogland, K.S. Jeong, H. Liu, L. Levina, M. Furukawa, X. Wang, R. Debnath, D. Cha, et al., Colloidal-quantum-dot photovoltaics using atomic-ligand passivation, Nat. Mater. (2011), https://doi.org/10.1038/nmat3118.

[14] H. Zhang, B. Hu, L. Sun, R. Hovden, F.W. Wise, D.A. Muller, R.D. Robinson, Surfactant ligand removal and rational fabrication of inorganically connected quantum dots, Nano Lett. (2011), https://doi.org/10.1021/nl202892p.

[15] A. Abelson, C. Qian, T. Salk, Z. Luan, K. Fu, J.-G. Zheng, J.L. Wardini, M. Law, Collective topo-epitaxy in the self-assembly of a 3D quantum dot superlattice, Nat. Mater. (2020), https://doi.org/10.1038/s41563-019-0485-2.

[16] Y. Liu, J. Tolentino, M. Gibbs, R. Ihly, C.L. Perkins, Y. Liu, N. Crawford, J.C. Hemminger, M. Law, PbSe quantum dot field-effect transistors with air-stable electron mobilities above 7 $cm^2 V^{-1} s^{-1}$, Nano Lett. (2013), https://doi.org/10.1021/nl304753n.

[17] K.S. Leschkies, M.S. Kang, E.S. Aydil, D.J. Norris, Influence of atmospheric gases on the electrical properties of PbSe quantum-dot films, J. Phys. Chem. C (2010), https://doi.org/10.1021/jp101695s.

[18] M. Sykora, A.Y. Koposov, J.A. McGuire, R.K. Schulze, O. Tretiak, J.M. Pietryga, V.I. Klimov, Effect of air exposure on surface properties, electronic structure, and carrier relaxation in PbSe nanocrystals, ACS Nano (2010), https://doi.org/10.1021/nn100131w.

[19] J. Tang, L. Brzozowski, D.A.R. Barkhouse, X. Wang, R. Debnath, R. Wolowiec, E. Palmiano, L. Levina, A.G. Pattantyus-Abraham, D. Jamakosmanovic, et al., Quantum Dot Photovoltaics in the Extreme Quantum Confinement Regime: The Surface-Chemical Origins of Exceptional Air- and Light-Stability, ACS Nano, 2010, https://doi.org/10.1021/nn901564q.

[20] I. Moreels, K. Lambert, D. De Muynck, F. Vanhaecke, D. Poelman, J.C. Martins, G. Allan, Z. Hens, Composition and size-dependent extinction coefficient of colloidal PbSe quantum dots, Chem. Mater. (2007), https://doi.org/10.1021/cm071410q.

[21] Ilavsky, J. Nika, Software for two-dimensional data reduction, J. Appl. Crystallogr. (2012), https://doi.org/10.1107/s0021889812004037.

[22] S.R. Kline, Reduction and analysis of SANS and USANS data using IGOR pro, J. Appl. Crystallogr. (2006), https://doi.org/10.1107/s0021889806035059.

[23] R.M. Feenstra, Tunneling spectroscopy of the (110) surface of direct-Gap III-V semiconductors, Phys. Rev. B (1994), https://doi.org/10.1103/PhysRevB.50.4561.

[24] R.M. Feenstra, J.Y. Lee, M.H. Kang, G. Meyer, K.H. Rieder, Band Gap of the Ge (111) c (2×8) Surface by Scanning Tunneling Spectroscopy, Phys. Rev. B - Condens. Matter Mater. Phys. (2006), https://doi.org/10.1103/PhysRevB.73.035310.

[25] J.M. Luther, M. Law, M.C. Beard, Q. Song, M.O. Reese, R.J. Ellingson, A.J. Nozik, Schottky solar cells based on colloidal nanocrystal films, Nano Lett. (2008), https://doi.org/10.1021/nl802476m.

[26] Y. Wang, X. Peng, A. Abelson, P. Xiao, C. Qian, L. Yu, C. Ophus, P. Ercius, L.-W. Wang, M. Law, H. Zheng, Dynamic deformability of individual PbSe nanocrystals during superlattice phase transitions, Sci. Adv. 5 (2019) (6), https://doi.org/10.1126/sciadv.aaw5623.

[27] W.J. Baumgardner, K. Whitham, T. Hanrath, Confined-but-connected quantum solids via controlled ligand displacement, Nano Lett. (2013), https://doi.org/10.1021/nl401298s.
[28] W.H. Evers, B. Goris, S. Bals, M. Casavola, J. De Graaf, R.Van Roij, M. Dijkstra, D. Vanmaekelbergh, Low-dimensional semiconductor superlattices formed by geometric control over nanocrystal attachment, Nano Lett. (2013), https://doi.org/10.1021/nl303322k.
[29] T. Tiedje, J. Varon, H. Deckman, J. Stokes, Tip contamination effects in ambient pressure scanning tunneling microscopy imaging of graphite, J. Vac. Sci. Technol. A Vacuum, Surfaces, Film. (2002), https://doi.org/10.1116/1.575418.
[30] D.V. Talapin, C.B. Murray, Applied Physics: PbSe Nanocrystal Solids for n- and p-Channel Thin Film Field-Effect Transistors, Science (80-.) (2005), https://doi.org/10.1126/science.1116703.
[31] D. Kim, D.H. Kim, J.H. Lee, J.C. Grossman, Impact of stoichiometry on the electronic structure of PbS quantum dots, Phys. Rev. Lett. (2013), https://doi.org/10.1103/PhysRevLett. 110.196802.
[32] T. Kaufman-Osborn, E.A. Chagarov, A.C. Kummel, Atomic imaging and modeling of H2O2(g) surface passivation, functionalization, and atomic layer deposition nucleation on the Ge(100) surface, J. Chem. Phys. (2014), https://doi.org/10.1063/1.4878496.
[33] D. Zhitomirsky, I.J. Kramer, A.J. Labelle, A. Fischer, R. Debnath, J. Pan, O.M. Bakr, E.H. Sargent, Colloidal quantum dot photovoltaics: the effect of polydispersity, Nano Lett. (2012), https://doi.org/10.1021/nl2041589.
[34] P. Nagpal, V.I. Klimov, Role of mid-gap states in charge transport and photoconductivity in semiconductor nanocrystal films, Nat. Commun. (2011), https://doi.org/10.1038/ncomms1492.
[35] D. Zhitomirsky, M. Furukawa, J. Tang, P. Stadler, S. Hoogland, O. Voznyy, H. Liu, E.H. Sargent, n-Type colloidal-quantum-dot solids for photovoltaics, Adv. Mater. (2012), https://doi.org/10.1002/adma.201202825.
[36] G. Konstantatos, L. Levina, A. Fischer, E.H. Sargent, Engineering the temporal response of photoconductive photodetectors via selective introduction of surface trap states, Nano Lett. (2008), https://doi.org/10.1021/nl080373e.
[37] M.H. Zarghami, Y. Liu, M. Gibbs, E. Gebremichael, C. Webster, M. Law, p-Type PbSe and PbS quantum dot solids prepared with short-chain acids and diacids, ACS Nano (2010), https://doi.org/10.1021/nn100339b.
[38] N. Zhao, T.P. Osedach, L.Y. Chang, S.M. Geyer, D. Wanger, M.T. Binda, A.C. Arango, M.G. Bawendi, V. Bulovic, Colloidal PbS quantum dot solar cells with high fill factor, ACS Nano (2010), https://doi.org/10.1021/nn100129j.
[39] Y. Zhang, D. Zherebetskyy, N.D. Bronstein, S. Barja, L. Lichtenstein, A.P. Alivisatos, L.W. Wang, M. Salmeron, Molecular oxygen induced in-gap states in PbS quantum dots, ACS Nano (2015), https://doi.org/10.1021/acsnano.5b04677.
[40] J.M. Luther, M. Law, Q. Song, C.L. Perkins, M.C. Beard, A.J. Nozik, Structural, Optical, and electrical properties of self-assembled films of PbSe nanocrystals treated with 1,2-ethanedithiol, ACS Nano (2008), https://doi.org/10.1021/nn7003348.
[41] S.J. Oh, D.K. Kim, C.E.R. Kagan, Remote doping and schottky barrier formation in strongly quantum confined single PbSe nanowire field-effect transistors, ACS Nano (2012), https://doi.org/10.1021/nn3009382.
[42] C. Adelmann, D. Cuypers, M. Tallarida, L.N.J. Rodriguez, A. De Clercq, D. Friedrich, T. Conard, A. Delabie, J.W. Seo, J.P. Locquet, et al., Surface chemistry and interface formation during the atomic layer deposition of alumina from trimethylaluminum and water on indium phosphide, Chem. Mater. (2013), https://doi.org/10.1021/cm304070h.
[43] V.V. Tomaev, L.L. Makarov, P.A. Tikhonov, A.A. Solomennikov, Oxidation kinetics of lead selenide, Glas. Phys. Chem. (2004), https://doi.org/10.1023/B:GPAC.0000038709.80613.51.
[44] C. Gautier, M. Cambon-Muller, M. Averous, Study of PbSe layer oxidation and oxide dissolution, Appl. Surf. Sci. (1999), https://doi.org/10.1016/S0169-4332(98)00606-0.
[45] M. Tallarida, C. Adelmann, A. Delabie, S. Van Elshocht, M. Caymax, D. Schmeisser, Surface chemistry and fermi level movement during the self-cleaning of GaAs by trimethyl-aluminum, Appl. Phys. Lett. (2011), https://doi.org/10.1063/1.3615784.
[46] C.L. Hinkle, A.M. Sonnet, E.M. Vogel, S. McDonnell, G.J. Hughes, M. Milojevic, B. Lee, F.S. Aguirre-Tostado, K.J. Choi, H.C. Kim, J. Kim, R.M. Wallace, GaAs interfacial self-cleaning by atomic layer deposition, Appl. Phys. Lett. (2008), https://doi.org/10.1063/1.2883956.
[47] H.D. Trinh, E.Y. Chang, Y.Y. Wong, C.C. Yu, C.Y. Chang, Y.C. Lin, H.Q. Nguyen, B.T. Tran, Effects of wet chemical and trimethyl aluminum treatments on the interface properties in atomic layer deposition of Al_2O_3 on InAs, Jpn. J. Appl. Phys. (2010), https://doi.org/10.1143/JJAP.49.111201.
[48] M. Milojevic, R. Contreras-Guerrero, M. Lopez-Lopez, J. Kim, R.M. Wallace, Characterization of the “Clean-up” of the Oxidized Ge(100) Surface by Atomic Layer Deposition, Appl. Phys. Lett. (2009), https://doi.org/10.1063/1.3268449.
[49] T.P. Osedach, N. Zhao, T.L. Andrew, P.R. Brown, D.D. Wanger, D.B. Strasfeld, L.Y. Chang, M.G. Bawendi, V. Bulović, Bias-stress effect in 1,2-ethanedithiol-treated PbS quantum dot field-effect transistors, ACS Nano (2012), https://doi.org/10.1021/nn3008788.
[50] Y. Liu, M. Gibbs, J. Puthussery, S. Gaik, R. Ihly, H.W. Hillhouse, M. Law, Dependence of carrier mobility on nanocrystal size and ligand length in PbSe nanocrystal solids, Nano Lett. (2010), https://doi.org/10.1021/nl101284k.
[51] J.H. Choi, A.T. Fafarman, S.J. Oh, D.K. Ko, D.K. Kim, B.T. Diroll, S. Muramoto, J.G. Gillen, C.B. Murray, C.R. Kagan, Bandlike transport in strongly coupled and doped quantum dot solids: a route to high-performance thin-film electronics, Nano Lett. (2012), https://doi.org/10.1021/nl301104z.
[52] D. Zherebetskyy, M. Scheele, Y. Zhang, N. Bronstein, C. Thompson, D. Britt, M. Salmeron, P. Alivisatos, L.W. Wang, Hydroxylation of the surface of PbS nanocrystals passivated with oleic acid, Science (80-.) (2014), https://doi.org/10.1126/science.1252727.